Editors' Suggestion

Spin- to charge-current conversion in altermagnetic candidate RuO_2 probed by terahertz emission spectroscopy

J. Jechumtál,[1] O. Gueckstock,[2] K. Jasenský,[1] Z. Kašpar,[1,3] K. Olejník,[3] M. Gaerner,[4] G. Reiss,[4] S. Moser,[5] P. Kessler,[5] G. De Luca,[6] S. Ganguly,[7] J. Santiso,[7] D. Scheffler,[3] J. Zázvorka,[1] P. Kubaščík,[1] H. Reichlová,[3] E. Schmoranzerová,[1] P. Němec,[1] T. Jungwirth,[3,8] P. Kužel,[3] T. Kampfrath,[2] and L. Nádvorník[1,*]

[1]*Faculty of Mathematics and Physics, Charles University, 121 16 Prague, Czech Republic*
[2]*Department of Physics, Freie Universität Berlin, 14195 Berlin, Germany*
[3]*Institute of Physics, Czech Academy of Science, 16200 Prague, Czech Republic*
[4]*Bielefeld University, Faculty of Physics, 33615 Bielefeld, Germany*
[5]*Physikalisches Institut and Würzburg-Dresden Cluster of Excellence ct.qmat, Universität Würzburg, 97074 Würzburg, Germany*
[6]*Materials Science Institute of Barcelona (ICMAB-CSIC), 08193 Barcelona, Spain*
[7]*Catalan Institute of Nanoscience and Nanotechnology (ICN2-CSIC-UAB) 08193 Barcelona, Spain*
[8]*School of Physics and Astronomy, University of Nottingham, United Kingdom*

(Received 18 August 2025; revised 1 December 2025; accepted 28 January 2026; published 23 February 2026)

Using the THz emission spectroscopy, we investigate ultrafast spin-to-charge current conversion in epitaxial thin films of the altermagnetic candidate RuO_2. We perform a quantitative analysis of competing effects that can contribute to the measured anisotropic THz emission. These include the anisotropic inverse spin splitter and spin Hall effects in RuO_2, the anisotropic conductivity of RuO_2, and the birefringence of the TiO_2 substrate. We observe that the leading contribution to the measured signals comes from the anisotropic inverse spin Hall effect, with an average spin-Hall angle of 2.4×10^{-3} at room temperature. In comparison, a possible contribution from the altermagnetic inverse spin-splitter effect is found to be approximately $2–4\times10^{-4}$. Our work stresses the importance of carefully disentangling spin-dependent phenomena that can be generated by the unconventional altermagnetic order, from the effects of the relativistic spin-orbit coupling.

DOI: 10.1103/d17q-1lg4

Altermagnetism has recently emerged as a new symmetry class in magnetism [1], characterized by a momentum-dependent alternating spin polarization in the reciprocal space of collinear, magnetically compensated systems. Unlike conventional ferromagnets or antiferromagnets, the altermagnetic order spontaneously breaks both spin-space and real-space rotation symmetries, while preserving a symmetry combining spin-space and real-space rotation transformations. This property gives rise to unconventional spin transport, such as the spin-splitter effect, giant magneto-transport anisotropies, and spin-polarized currents without net magnetization [2,3]. Among the broad class of proposed altermagnets, rutile-structured RuO_2 stands out as a particularly compelling candidate [2,4,5]. In the altermagnetic phase, it is predicted to combine metallic conductivity with d-wave-type spin order, all in a simple binary compound [1–5], making it an ideal platform for both theoretical and experimental investigations.

RuO_2 has long been known as a nonmagnetic, versatile material, useful in electrochemistry and electronics [6], yet it has been going through a dynamic experimental development in recent years. After reports indicating a presence of a compensated collinear magnetic order, based on neutron diffraction [7] and x-ray scattering [8], several transport experiments showed signals suggestive of a theoretically predicted [4] altermagnetic anomalous Hall [9], a theoretically predicted [10] spin-splitter effect (SSE) measured via a GHz ferromagnetic resonance [11–13], and an inverse spin-splitter effect (ISSE) detected by a DC spin Seebeck effect [14] or by THz emission [15]. However, the consensus on the magnetic ordering of RuO_2 has been recently challenged by muon spin rotation [16], neutron scattering [17], and angle-resolved photoemission spectroscopy (ARPES) [18] studies reporting no magnetic order in the studied samples. The ongoing debate on altermagnetism in RuO_2 involves, on one hand, additional observations attributed to the altermagnetic order, including the tunneling magnetoresistance [19], the anomalous Hall effect [20,21], the spin-split band structure measured by ARPES [22], the DC SSE-induced switching of an adjacent magnet [23], or the optically induced spin polarization [24]. On the other hand, recent thermal-transport [25] and spin-pumping [26] studies attributed the observed spin-to-charge conversion to an anisotropic inverse spin Hall effect (ISHE), rather than the ISSE. Similarly, a recent THz-emission study did not find evidence for the ISSE, and ascribed the observed signals to the anisotropic conductivity of RuO_2 [27]. Therefore it is crucial for the current discussion to scrutinize experimental data by considering all other competing effects that may mimic the altermagnetic (I)SSE by sharing analogous experimentally observable symmetries.

In this paper, we provide an ultrafast probe of the spin-to-charge current conversion in RuO_2-based multilayers by the time-domain THz emission spectroscopy. It is a natural tool for probing processes with expected ultrafast dynamics, as

*Contact author: lukas.nadvornik@matfyz.cuni.cz

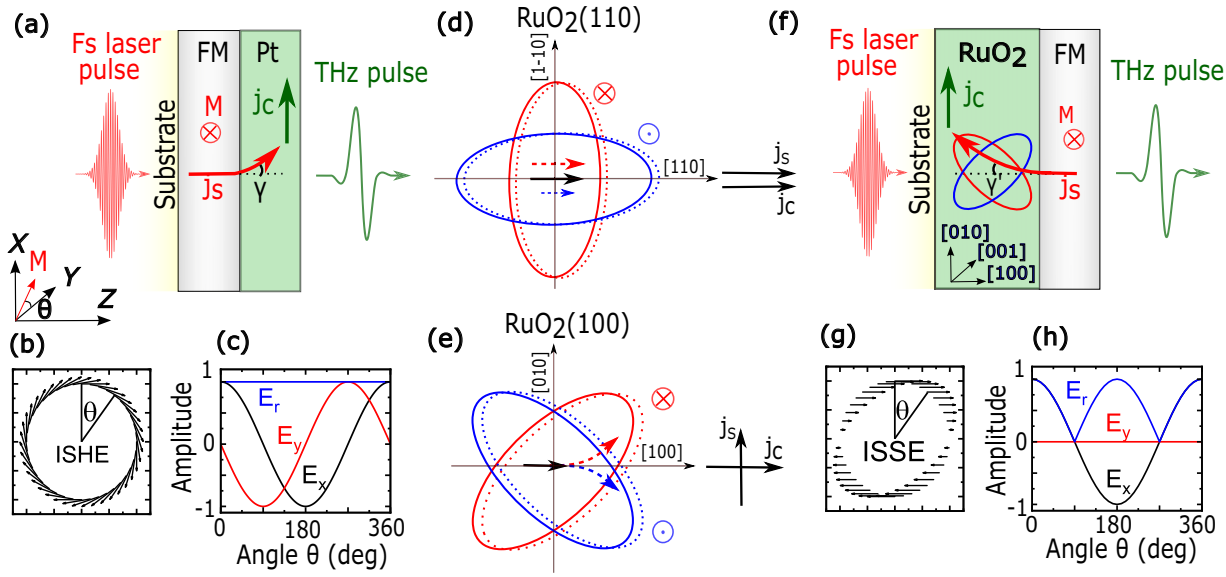

FIG. 1. THz emission from FM|Pt, FM|RuO_2 and symmetry of spin splitter effect (SSE). (a) Spintronic terahertz emission from a reference bilayer ferromagnet (FM)|Pt. A femtosecond laser pulse excites the FM with in-plane magnetization $\boldsymbol{M}$ and, thus, injects a spin current $\boldsymbol{j}_s$ (red arrow) into Pt, where it is converted into a transverse charge current $\boldsymbol{j}_c$ (green arrow) by the ISHE, with an efficiency defined by the angle $\boldsymbol{\gamma}$. Consequently, a THz electromagnetic pulse is radiated. When changing the angle θ of $\boldsymbol{M}$ in the x-y plane by an external magnetic field, (b) the emitted electric field $\boldsymbol{E}$ is always perpendicular to $\boldsymbol{M}$ and has identical amplitudes and waveforms, resulting in (c) the typical harmonic projections E_x, E_y, and the constant total magnitude E_r. [(d) and (e)] Symmetry of altermagnetic SSE. (d) Sending $\boldsymbol{j}_c$ along [110] crystal direction of a d-wave altermagnet leads to spin polarization of current, but no generation of any transversal component of $\boldsymbol{j}_s$ to the direction of $\boldsymbol{j}_c$. (e) $\boldsymbol{j}_c$ sent along [100] crystal direction leads to spin-dependent deflection of up and down spins, which translates to the transversal $\boldsymbol{j}_s$. The inverse equivalent, where $\boldsymbol{j}_s$ produces transversal $\boldsymbol{j}_c$, is dubbed the inverse spin splitter effect (ISSE). (f) THz emission from RuO_2(100)|FM with potential altermagnetic ISSE, acting analogously to ISHE in (a). $\theta = 0$ corresponds to $\boldsymbol{M} \parallel$ [001] direction of RuO_2. (g), (h) Analogous projections of the ISSE-driven emitted $\boldsymbol{E}$. Unlike (b) and (c), $E_y = 0$ because y axis is set along the [001] direction of RuO_2. This is also the direction in which the Neél vector lies and, consequently, no spin splitting is expected. Moreover, E_r is not constant as the projection of the injected spin to [001] direction of RuO_2 is varying with angle θ.

it can infer, unlike transport and low- frequency techniques, the dynamics and potential speed limits of the studied phenomenon [28–30]. By considering three possible sources of competing signals to the anisotropic ISSE—the anisotropic ISHE in RuO_2, the anisotropic conductivity of RuO_2, and the birefringence of the TiO_2 substrate, we analyze the strongly anisotropic THz emission in a quantitative way by a comparison to the emission model. The nearly perfect match of our calculations with the measured data allows us to infer the magnitude and polarity of the isotropic part of the ISHE and to demonstrate a strong, anisotropic component of the ISHE in the THz range. From our analysis of the measured data at room temperature, we conclude that the ISSE angle is approximately $2\text{–}4\times10^{-4}$. This is three orders of magnitude smaller than the zero-temperature theoretical value considering a single domain altermagnetic state of RuO_2 [10,2].

The experiment follows the emission scheme from spintronic THz emitters [Fig. 1(a)] [31]. Here, an ultrashort laser pulse excites a bilayer consisting of a ferromagnetic-metal layer FM and a heavy-metal layer HM, for example, Pt. The optical heating generates a transient spin voltage in FM and, thus, drives a spin current with density $\boldsymbol{j}_s$ across the FM/HM interface [32]. The spin orientation of $\boldsymbol{j}_s$ is determined by the direction of the in-plane magnetization $\boldsymbol{M}$ of FM. Inside HM, $\boldsymbol{j}_s$ is converted to an in-plane charge current with density $\boldsymbol{j}_c$ via the ISHE. Finally, the total emitted field $\boldsymbol{E}$ directly behind the sample corresponds to the total integrated charge current $\boldsymbol{I}_c = \int \boldsymbol{j}_c(z)dz$ [30,33]:

$$\boldsymbol{E} = eZ\boldsymbol{I}_c \propto eZ\gamma \boldsymbol{I}_s \times \boldsymbol{e}_M, \tag{1}$$

where e is the elementary charge, Z is the sample impedance, γ is the spin-Hall angle, $\boldsymbol{I}_s = \int \boldsymbol{j}_s(z)\mathrm{d}z$ is the total integrated spin current, $\boldsymbol{e}_M$ is the unit vector in the direction of $\boldsymbol{M}$, and the ISHE is isotropic. It follows from the cross product in Eq. (1) that the emitted $\boldsymbol{E}$ is perpendicular to $\boldsymbol{M}$ and forms an isotropic texture [Fig. 1(b)] if $\boldsymbol{M}$ is rotated by an angle θ. Correspondingly, the x and y components of $\boldsymbol{E}$ follow the harmonic θ dependence, $E_x \propto \cos\theta$ and $E_y \propto -\sin\theta$, while the magnitude $E_r = |\boldsymbol{E}|$ is constant [Fig. 1(c)].

If we replace HM = Pt by a suitably oriented d-wave altermagnet, in our case (100)-grown RuO_2 in the altermagnetic phase, we expect the ISSE [Figs. 1(d) and 1(e)]. This phenomenon, together with its complementary spin-polarization effect, are theoretically predicted to arise from a spin-split band-structure the polarity of which alternates in the [110] and [1–10] crystal directions of RuO_2 [10]. The spin-polarizer effect arises if an electric current $\boldsymbol{j}_c$ is sent along one of these directions and the current is spin-polarized due to the difference in the Fermi surfaces for spin up and down [Fig. 1(d)]. However, the spin-splitter effect appears when $\boldsymbol{j}_c$ is applied along a nodal direction [100] or [010] and a transversal spin current $\boldsymbol{j}_s$ arises as a consequence of anisotropic spin splitting [Fig. 1(e)], leading to spin-dependent deflection of electrons. The inverse analog of the latter phenomenon is dubbed ISSE.

The spin-to-charge current conversion due to it is represented by the angle γ' and is added to the ISHE in the emission scheme described above [Fig. 1(f)].

Since the direction of the spin-to-charge current conversion due to the ISSE is determined by the fixed crystal orientation, the emission texture is anisotropic. If we set $\theta = 0°$ for $\boldsymbol{M} \parallel y$, i.e., the [001] direction of RuO_2, we expect only the y projection of the injected spin to contribute to E_x of the emission texture and its θ dependence as shown in Figs. 1(g) and 1(h). Notably, $E_x \propto \cos\theta$, $E_y = 0$ and $E_r \propto |\cos\theta|$, which allows us to disentangle the isotropic ISHE and the anisotropic ISSE. From these considerations, we can formulate two basic criteria to confirm the presence of the ISSE in RuO_2-based samples: (1) the THz emission from $RuO_2(100)$ must be consistent with the texture in Fig. 1(g). (2) This contribution must vanish in RuO(110), where no ISSE signal is theoretically expected from symmetry, Fig. 1(e) [2,10] and used for interpretation of experiments [11,12,14].

These criteria dictate the choice of our samples: 10-nm-thick (100) or (110)-oriented RuO_2 grown on a (100) or (110)-oriented TiO_2 substrate, followed by 2.5 nm of ferromagnetic $Co_{40}Fe_{40}B_{20}$, capped by 3 nm of Si (see Supplemental Material note 1 for more sample characterization [34]). As a reference sample, we use the same FM layer grown on $TiO_2(100)$, capped by 2.5 nm of Pt. The in-plane orientation of the CoFeB magnetization is controlled by a rotatable external magnetic field of strength of 350 mT, which is more than an order of magnitude larger than the saturation field of the FM layers (see Supplemental Material, Fig. S5) [34]. To excite the thin-film stacks, we use femtosecond laser pulses generated in a regenerative amplifier (pulse duration 170 fs, energy 30 μJ, repetition rate 10 kHz). The emitted THz field components E_x and E_y are probed by electro-optic (EO) sampling [35,36] in a 2-mm-thick GaP(110) detection crystal using two THz polarizers, resulting in EO signals S_x^{EO} and S_y^{EO}. All experiments are performed in a dry-air atmosphere and at room temperature.

The typical $\boldsymbol{M}$-dependent THz waveforms $S_x(t)$ and $S_y(t)$ from our samples, after subtraction of the θ-averaged, non-magnetic signal from S_x^{EO} and S_y^{EO}, are shown in Figs. 2(a) and 2(b). While the signal from the CoFeB|Pt reference sample (magenta curves) shares practically identical temporal dynamics in both x and y projections, the signal from RuO_2|CoFeB (red and blue curves) shows a notable difference. Mainly, $S_y(t)$ has a more bipolar character, whereas $S_x(t)$ is more unipolar, similar to signals from CoFeB|Pt. This behavior suggests that the spin-to-charge conversion process may partly have a different origin. The full θ dependence of signals is shown for (100)-RuO2|CoFeB by a sequence of 40 colors.

Further, we measure the θ dependence of $S(t)$ for all samples (shown in Fig. 2 by a sequence of 40 colors and S1) [34], compute the root-mean-square (RMS) of the waveforms, multiplied by the sign of the signal at the main waveform peak, and plot them in the form of emission textures [Figs. 3(a), 3(c), and 3(e)] and of the corresponding $S_x(\theta)$, $S_y(\theta)$, and $S_r(\theta)$ projections [Figs. 3(b), 3(d), and 3(f)]. We note that RMS is a convenient way to determine the signal strength as it is less prone to single-data-point noise as compared to the peak-to-peak value. Without any quantitative analysis, we see that all the emission textures are not fully isotropic, as

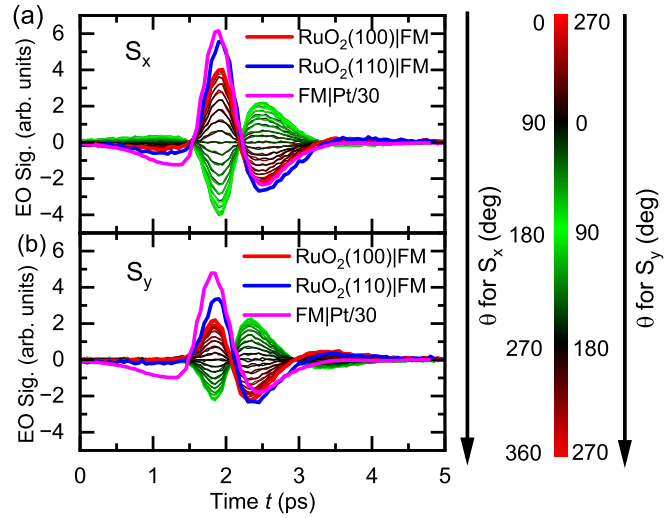

FIG. 2. Typical THz-emission signals. (a) The x-projection $S_x(t)$ of the EO signals from $RuO_2(100)$|CoFeB (red), $RuO_2(110)$|CoFeB (blue), and reference sample CoFeB|Pt (magenta, rescaled by an indicated factor of 30) for $\theta = 0°$. (b) The same dataset for $S_y(t)$ and $\theta = 270°$. An example of the typical full θ dependence is shown for (100)-RuO_2|CoFeB (sequence of 40 colors shown in color map on right side).

expected from the purely isotropic-ISHE-driven conversion [cf. Figs. 1(b) and 1(c)]. To highlight the differences, we model the isotropic contribution by fitting S_y by a harmonic function, $S_y' = -A_i \sin\theta$, where A_i with i = Pt, (110), (100) is the amplitude of the isotropic conversion for the reference CoFeB|Pt and the respective orientation of RuO_2|CoFeB samples. Subsequently, we plot the corresponding x projection, $S_x' = A_i \cos\theta$, and the magnitude of the emission $S_r' = A_i$ [curves in Figs. 3(b), 3(d), and 3(f)], and shade the difference between the model and the experimental data. The best-fit parameters $A_{(100)} = 0.024 A_{Pt}$ and $A_{(110)} = 0.031 A_{Pt}$ allow us to estimate the effective spin Hall angle γ_{RuO2} of the isotropic conversion in RuO_2 by a comparison to A_{Pt} of the reference sample. By assuming that the total conversion is dominated by the conversion inside RuO_2 and $\gamma_{Pt} = 10^{-1}$ [37–41] (see Supplemental Material note 2 for more details [34]), we obtain $\gamma_{RuO_2} = -(2.1 \pm 0.2)\times 10^{-3}$ and $-(2.7 \pm 0.2)\times 10^{-3}$ for the (100) and (110)-oriented sample, respectively. Note that the negative sign of γ_{RuO_2} comes from the fact that the signal polarity is the same as for CoFeB|Pt (Fig. 2), but the layer order of the FM|HM stacks is reversed (Fig. 1).

The additional conversion contributions are analyzed by subtraction of the isotropic model from the data, i.e., $\Delta S_x = S_x - S_x'$ and $\Delta S_y = S_y - S_y'$, and by normalizing them to the corresponding A_i, as shown in Fig. 4. The residual emission textures [(a), (c), and (e)] and their projections [(b), (d), and (f)] follow an ISSE-like pattern [Figs. 1(d) and 1(f)] in all three samples. Remarkably, the modulation depth of $\Delta S_x/A_i$, which quantifies the anisotropic emission, reaches $(46 \pm 1)\%$ and $(53 \pm 1)\%$ for (100)-RuO_2 and (110)-RuO_2, respectively, and $(28.8 \pm 0.3)\%$ for the reference sample. The very similar modulation strengths in both orientations (100) and (110) of RuO_2 clearly violate the criterion (2). The small difference

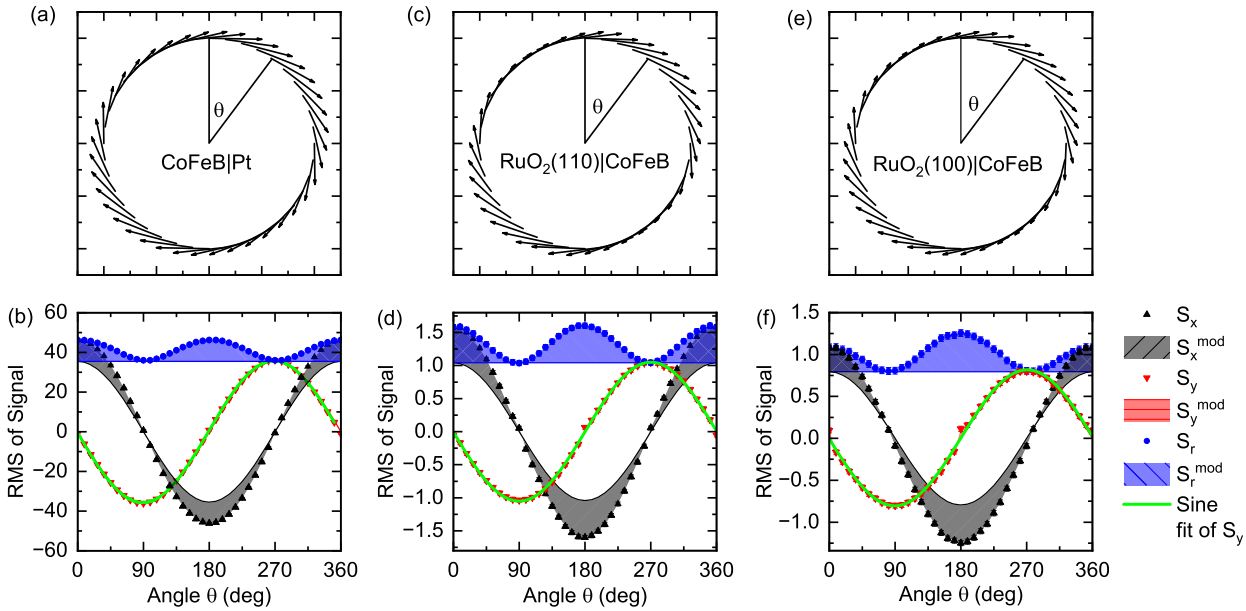

FIG. 3. Analysis of θ dependence. (a) RMS of S_x and S_y as a function of θ as a texture plot for the CoFeB|Pt reference sample. (b) RMS of the measured components $S_x(\theta)$, $S_y(\theta)$, and of the magnitude $S_r(\theta)$ (symbols) compared with the model (lines) by Eq. (1) using only the isotropic ISHE contribution. Here, $S_y(\theta)$ is fit by $A \sin\ \theta$ [Eq. (1), green curve], and the shaded areas for $S_x(\theta)$ and $S_r(\theta)$ highlight the difference between the experiment and the isotropic model. (c), (d) Analogous analysis for $RuO_2(110)$|CoFeB, where no ISSE is expected, and (e), (f) for $RuO_2(100)$|CoFeB sample, where the ISSE is allowed. Notice that textures in (a), (c) and (e) are based on the same underlying data as shown in (b), (d) and (f), both providing different views on signal symmetries and their amplitudes.

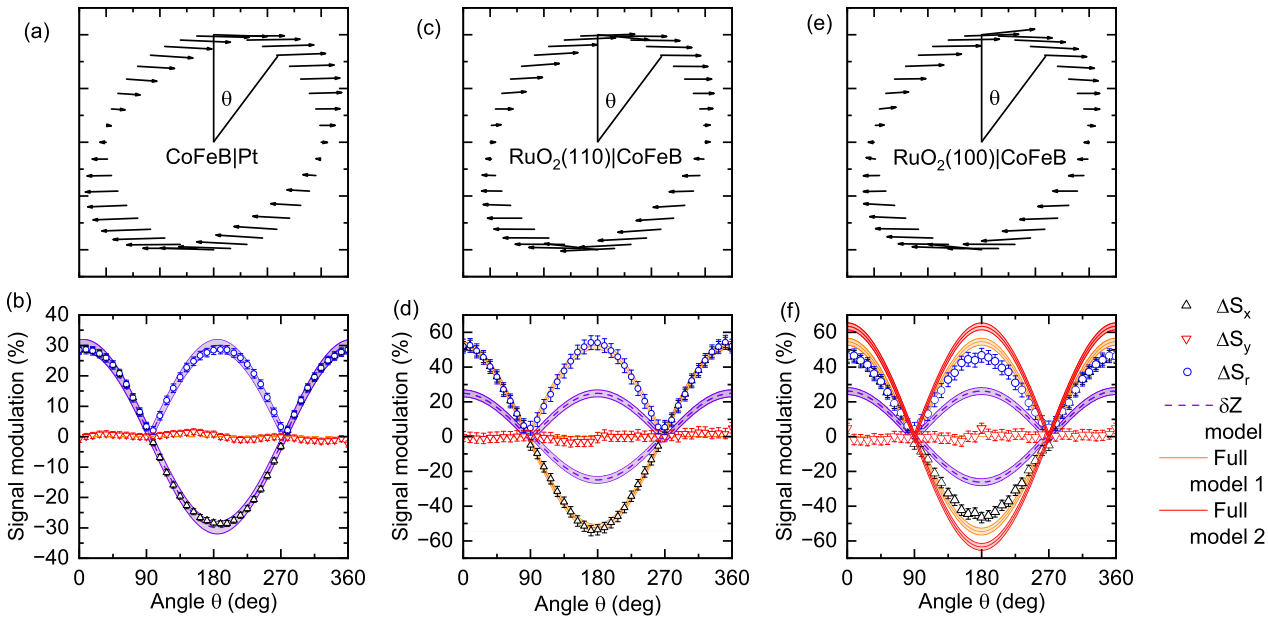

FIG. 4. Modulation of θ dependence. [(a) and (b)] CoFeB|Pt sample. (a) Emission texture after subtraction of isotropic ISHE contribution. (b) Residuals $\Delta S_x(\theta)$, $\Delta S_y(\theta)$, $\Delta S_r(\theta)$ from (a), normalized to A (symbols), compared to the model of anisotropic outcoupling part of Eq. (2), i.e., only $\delta Z/Z_y \neq 0$ (violet dashed curve). [(c) and (d)] Analogous analysis for (110)-RuO_2|CoFeB sample, the ISSE inactive orientation. [(e) and (f)] Analogous for (100)-RuO_2|CoFeB sample, the ISSE active orientation. In (d) and (f), we complement the partial model (only $\delta Z/Z_y \neq 0$, violet dashed curve) with the full models by whole Eq. (2) including anisotropic ISHE. Model 1 assumes different spin transparency between the two RuO_2 samples (orange curve), model 2 assumes different conversion in the FM layer (red curve). See the main text for a detailed description of the modeling procedure. Notice that textures in (a), (c), and (e) are based on the same underlying data as shown in (b), (d), and (f).

in the modulations indicates that a possible contribution of the ISSE remains very limited in our measurements, with an upper bound of several percent of the magnitude of the isotropic ISHE conversion.

Next, we investigate the sources of anisotropies in emission that may appear in our samples. First, the used TiO_2 substrate exhibits a very strong birefringence in the THz spectral range [42,43], which affects the outcoupling of the THz radiation from the sample. As anticipated by Eq. (1), the outcoupling is characterized by the sample impedance Z, which can be modeled in the thin-film approximation [29,44] as $Z \approx Z_0/(1 + n_s + Z_0 G)$. Here, $Z_0 \approx 377\ \Omega$ is the vacuum impedance, n_s the refractive index of the substrate in the polarization direction of E, and G is the THz conductance of the conductive layers. We directly measured the two principal values of n_s in uniaxial TiO_2 substrates in the THz range (see Fig. S2 [34]), showing no significant spectral dependence and yielding $n_{s,x} = 9.5 \pm 0.1$ and $n_{s,y} = 12.9 \pm 0.1$, respectively. The substrate birefringence leads to an anisotropic impedance: $Z_x = Z_y + \delta Z$, and accounts for its notable relative variation $\delta Z/Z_y = (26 \pm 1)\%$ for the average G of our samples.

Another source of anisotropic outcoupling could be the anisotropic G of the conductive layer itself, which was suspected to cause the anisotropic THz emission from RuO_2-based samples in Ref. [27]. However, using THz transmission experiments, we did not observe any large variation of G in our samples as $\delta G/G_y \approx 1.4\%$ and -4.3% for (100)- and (110)-RuO_2|CoFeB, respectively, while in the case of CoFeB|Pt we inferred $\delta G/G_y \approx 18.6\%$ (see Supplemental Material, Table T1 [34]).

The third potential source is the recently suggested anisotropy of the spin Hall angle in (100) and (110)-oriented RuO_2, which was evaluated by DC spin Seebeck experiments to $\delta\gamma/\gamma_y \approx 30\%$ [25]. Using the above-mentioned anisotropies, we can model the anisotropic emission by separating the x and y components of the emitted E and expanding Eq. (1) as follows (see Supplemental Material note 3):

$$\begin{pmatrix} E_x \\ E_y \end{pmatrix} = e\begin{pmatrix} Z_x \boldsymbol{I}_{c,x} \\ Z_y \boldsymbol{I}_{c,y} \end{pmatrix} \propto \begin{pmatrix} Z_x(\gamma_x + \gamma')\cos\theta \\ Z_y\gamma_y(-\sin\theta) \end{pmatrix} = Z_y\gamma_y\left[\begin{pmatrix} \cos\theta \\ -\sin\theta \end{pmatrix} + \begin{pmatrix} \delta\gamma/\gamma_y + \gamma'/\gamma_y + \delta Z/Z_y + \Delta \\ 0 \end{pmatrix}\cos\theta\right]. \tag{2}$$

Here, both the x and y components include their respective outcoupling Z, the spin Hall angle γ is anisotropic, and γ' contributes only to E_x. The first term after the last equality is the isotropic conversion due to the isotropic ISHE, the second one is the correction due to anisotropies and possible ISSE, while $\Delta = (\delta Z/Z_y)(\delta\gamma/\gamma_y) + (\delta Z/Z_y)(\gamma'/\gamma_y)$ are less significant second-order terms. We see from Eq. (2) that all anisotropies contribute to the correction with the identical symmetry as the ISSE and, therefore, this altermagnetic feature cannot be separated based solely on the θ dependence of the THz emission from one sample.

Therefore we can compare the THz emission from all three samples with the model by plotting the anisotropic term of Eq. (2) on top of the measured data in Figs. 4(b), 4(d), and 4(f). First, we consider only the outcoupling anisotropy $\delta Z/Z_y$ and assume $\gamma' = \delta\gamma = 0$ (dashed violet curves). We observe a perfect match in the case of the reference sample, CoFeB|Pt, which is consistent with the expectation that Pt does not show any anisotropic ISHE. On the other hand, the data from the RuO_2-based samples clearly cannot be explained just by the outcoupling anisotropies (i.e., δn_s and δG). However, once we also add the anisotropic ISHE and fit the modulation of (110)-RuO_2 (full orange curves), we obtain $\delta\gamma/\gamma_y = (23 \pm 2)\%$. This value is consistent with the recent experimental observation [25]. By considering the anisotropy $\delta\gamma/\gamma_y$ to be same in both RuO_2 samples, we use $\delta\gamma/\gamma_y$ obtained from (110)-RuO_2 also to model the response of (100)-RuO_2 (labeled model 1). Here, we see a very good match of the model with the measured data, showing a difference by $\sim 9\%$. From this observation and from the fitted isotropic $\gamma_y \sim 2.4\times10^{-3}$, we can infer the upper bound of the magnitude of the potential, area-averaged contribution of the ISSE to $\gamma' \approx 2\times10^{-4}$ in our (100)-RuO_2 sample at room temperature. This is three orders of magnitude lower than the theoretical prediction of the zero-temperature ISSE in the single-domain altermagnetic phase of RuO_2 [2,10]. In addition, the amplitude of the anisotropic emission from RuO_2-based samples tended to decrease in time, and it shows no observable change when heated by 40 °C above the room temperature (Supplemental Material, Fig. S3 [34]).

The approximate isotropic $\gamma_{RuO_2} = -(2.4 \pm 0.2)\times10^{-3}$, averaged over both orientations of our RuO_2 samples, deviates from values reported in previous experiments in Refs. [11–13,23,26], where it had the opposite sign and ranged from 1.5×10^{-2} to 4.5×10^{-2}. However, the polarity of our inferred SHE angle matches the recent study findings by Wang *et al.* in YIG/RuO_2 systems [25]. This work was performed on a large set of samples with an insulating ferrimagnetic layer, thus, without an additional contribution from the spin-to-change conversion in the magnet. The authors assign the overall positive polarity of the previous studies to this potential contribution of the positive SHE angle in metallic metals like NiFe and CoFeB [45,46]. Considering the generally lower γ_{FM} in $Co_{40}Fe_{40}B_{20}$ [46], it may explain our lower and negative value of γ. Other possible ISHE-like mechanisms contributing to the overall emission, originating in the ferromagnet, are the ultrafast demagnetization [32], the anomalous Hall effect [47] and anomalous Nernst effect [48]. All these mechanisms, summarized in an effective conversion angle γ_{FM}, are expected to be relatively weak in thin FM layers as compared to the leading mechanism, ISHE from RuO_2, and, more importantly, fully isotropic, as they are originating from the isotropic polycrystalline CoFeB layer. Therefore they could not contribute to the anisotropic parts of the conversion, the altermagnetic γ' or the anisotropic ISHE $\delta\gamma$. However, they can, in principle, contribute to the isotropic ISHE conversion γ_y itself. Additionally, the conversion by ISHE inside RuO_2 can be impacted by spin losses at the FM/RuO_2 inter-

face [37], resulting in its lower spin transparency t_s, or the Rashba-like conversion γ_I at the interface itself.

These probably small but potentially present contributions are generally difficult to be disentangled in THz emission experiments [37,49], and we advise to consider the isotropic part of γ the total effective conversion efficiency of the particular stack of layers:

$$\gamma_y = \gamma_{FM} + \gamma_I + t_s \gamma_{RuO_2}. \quad (3)$$

In Figs. 3(e) and 3(f), we see that the total isotropic conversion γ_y (i.e., the amplitude of S_y) varies by $\sim 20\%$ between the sample stack with (110)-RuO_2 and (100)-RuO_2. In the above estimate of the size, the altermagnetic conversion γ', we used the relative value of the anisotropic ISHE, $\delta\gamma/\gamma_y$, from (110)-RuO_2 sample in the model of emission from (100)-RuO_2 (model 1). This approach is immune to the variation of γ_y due to spin loss at the interface, which we consider the probable source of it, as t_s cancels in the term $\delta\gamma/\gamma_y$. However, we can explore the other extremal case when the difference of the isotropic γ_y is solely due to a change in γ_{FM} and γ_I, implying a variation of the CoFeB layer in these two stacks. To eliminate this effect from the analysis, one needs to use only $\delta\gamma$ from (110)-RuO_2 sample to model the conversion in (110)-RuO_2. This hypothetical situation leads to a proportionally larger modulation [model 2, see red curve in Fig. 4(f)] and yielding the maximal ISSE contribution $\gamma' \approx 4\times10^{-4}$. The realistic model, therefore, lies between models 1 and 2, giving the upper bound of γ' in the interval $(2-4)\times10^{-4}$.

The absence of a sizable ISSE in our samples at room temperature is the central conclusion of our paper. It is consistent with its absence reported by the very recent DC thermotransport [25] and THz emission experiments [27], and contrasts with the earlier SSE spin pumping studies at room temperature [11–13], where the authors inferred a magnitude of the SSE conversion in the same order as the SHE. Remarkably, experiments in Ref. [11] showed a strong temperature dependence of the SSE, which also contrasts with the negligible temperature dependence of our anisotropic signals (Supplemental Material, Fig. S3 [34]). Following the ongoing intense debate on the magnetic nature of RuO_2, there are two main explanations of our reported potential weak ISSE. (1) The magnetic domain structure can be formed with mutually compensating contributions to the ISSE. This argument was already used in Refs. [11,13] when explaining why the inferred ISSE reached only a fraction of the theoretically expected value [10]. (2) The debated nonmagnetic nature of RuO_2 at room temperature in bulk and thin layers [16–18]. Reflecting on the ongoing discussion of the magnetic order, we stress the relevance of our study with new insights in origin of anisotropic signals in RuO_2 and we suggest that future studies should include the THz emission experiments at lower temperatures [19,20] and in RuO_2 films of a variable disorder/impurity level [50] and thickness, including ultrathin, strained RuO_2 films with layer thicknesses below 2 nm [21,51]. The last-mentioned ultrathin strained films might be particularly interesting for the THz emission experiments, as this technique is interface sensitive and was successfully applied to nanometer-thin layers [37,49].

In summary, we performed THz-emission spectroscopy on RuO_2|CoFeB bilayers and studied the phenomenology of the spin-to-charge current conversion, with a particular focus on the observed anisotropic emission. To carefully analyze the data, we modeled the emission by considering the predicted altermagnetic contribution of the ISSE, together with three additional sources of analogous anisotropy: the birefringence of the substrate, the anisotropic ISHE, and the anisotropic conductivity of RuO_2. The modeling revealed that the anisotropic ISHE, recently proposed [26,25] due to the crystalline symmetry of RuO_2 and unprecedented in THz experiments, is indeed operative in the THz spectral range and that it reaches similarly large magnitude in both (100)- and (110)-grown RuO_2. This finding can have an application potential in devices that employ the transient spin accumulation or spin transfer torque, where the current direction can change the magnitude of the effect. Importantly, we observed no significant contribution of the altermagnetic ISSE at room temperature with a magnitude $(2-4)\times10^{-4}$. Our qualitative and quantitative understanding of the interplay of all sources of anisotropic THz emission is an important ingredient for the analysis and designs of future optical and THz experiments in RuO_2.

ACKNOWLEDGMENTS

The authors acknowledge funding by the Czech Science Foundation through projects GA CR (Grant No. 25–18281K), the Grant Agency of the Charles University (SVV–2024–260720), the Ministry of Education, Youth and Sports of the Czech Republic through the OP JAK call Excellent Research (TERAFIT Project No. CZ.02.01.01/00/22_008/0004594), CzechNanoLab Research Infrastructure supported by MEYS CR (LM2023051), the ERC-2023 Advanced Grant ORBITERA (Grant No. 101142285), the ERC-2023 Advanced Grant ALTERMAG (Grant No. 101095925), the ERC-2023 Proof-of-Concept Grant T-SPINDEX (Grant No. 101123255), the DFG Collaborative Research Center SFB TRR 227 "Ultrafast spin dynamics" (project ID 328545488, projects A05 and B02), the DFG Excellence Cluster EXC 3112 "Center for Chiral Electronics" (EXC 3112/1, Project No. 533767171) and the Research Unit RU 5844 ChiPS (Project No. 541503763). S.M. and P.Ke. received funding from the Deutsche Forschungsgemeinschaft (DFG, German Research Foundation) under Germany's Excellence Strategy through the Würzburg-Dresden Cluster of Excellence on Complexity and Topology in Quantum Matter ct.qmat (EXC 2147, Project ID 390858490) and through the Collaborative Research Center SFB 1170 ToCoTronics (Project ID 258499086), as well as from the New Zealand Ministry of Business, Innovation and Employment (MBIE, Grant No. C05×2004). H.R. to the Dioscuri Program LV23025 funded by Max Planck Society and MEYS of the Czech Republic. J.J. acknowledges the support by the Grant Agency of the Charles University (Grant No. 120324). P.K. acknowledges the support by the Grant Agency of the Charles University (Grant No. 166123). Z.K. acknowledges the European Union's Horizon Europe programme through project Tera-MaRs (No. 101211111). G.D.L. acknowledges Grant No. RYC2021-032524-I funded by MCIN/AEI/10.13039/501100011033 and by European Union NextGenerationEU/Plan de Recuperación, Transformación y Resiliencia. J.S. acknowledges the Severo Ochoa program from Spanish MCIN/AEI (Grant No.: CEX2021-001214-S). S.G. acknowledges the PREBIST Cofund grant. This project has received funding from the European Union's

Horizon 2020 research and innovation programme under the Marie Sklodowska-Curie Grant Agreement No. 754558. The authors acknowledge the networking opportunities provided by the European COST Action No. CA23136 (CHIROMAG).

DATA AVAILABILITY

The data that support the findings of this article are openly available [52].

[1] L. Šmejkal, J. Sinova, and T. Jungwirth, Beyond conventional ferromagnetism and antiferromagnetism: A phase with nonrelativistic spin and crystal rotation symmetry, Phys. Rev. X **12**, 031042 (2022).

[2] L. Šmejkal, J. Sinova, and T. Jungwirth, Emerging research landscape of altermagnetism, Phys. Rev. X **12**, 040501 (2022).

[3] L. Šmejkal, A. B. Hellenes, R. González-Hernández, J. Sinova, and T. Jungwirth, Giant and tunneling magnetoresistance in unconventional collinear antiferromagnets with nonrelativistic spin-momentum coupling, Phys. Rev. X **12**, 011028 (2022).

[4] L. Šmejkal, R. González-Hernández, T. Jungwirth, and J. Sinova, Crystal time-reversal symmetry breaking and spontaneous Hall effect in collinear antiferromagnets, Sci. Adv. **6**, eaaz8809 (2020).

[5] L. Šmejkal, A. Marmodoro, Kyo-Hoon Ahn, R. González-Hernández, I. Turek, S. Mankovsky, H. Ebert, S. W. D'Souza, O. Šipr, J. Sinova, and T. Jungwirth, Chiral magnons in altermagnetic RuO_2, Phys. Rev. Lett. **131**, 256703 (2023).

[6] S. Jayakumar, P. C. Santhosh, M. M. Mohideen, and A. V. Radhamani, A comprehensive review of metal oxides (RuO_2, Co_3O_4, MnO_2 and NiO) for supercapacitor applications and global market trends, J. Alloys Compd. **976**, 173170 (2024).

[7] T. Berlijn, P. C. Snijders, O. Delaire, H.-D. Zhou, T. A. Maier, H.-B. Cao, S.-X. Chi, M. Matsuda, Y. Wang, M. R. Koehler, P. R. C. Kent, and H. H. Weitering, Itinerant antiferromagnetism in RuO_2, Phys. Rev. Lett. **118**, 077201 (2017).

[8] Z. H. Zhu, J. Strempfer, R. R. Rao, C. A. Occhialini, J. Pelliciari, Y. Choi, T. Kawaguchi, H. You, J. F. Mitchell, Y. Shao-Horn, and R. Comin, Anomalous antiferromagnetism in metallic RuO_2 determined by resonant x-ray scattering, Phys. Rev. Lett. **122**, 017202 (2019).

[9] Z. Feng, X. Zhou, L. Šmejkal, L. Wu, Z. Zhu, H. Guo, R. González-Hernández, X. Wang, H. Yan, P. Qin, *et al.*, An anomalous Hall effect in altermagnetic ruthenium dioxide, Nat. Electron. **5**, 735 (2022).

[10] R. Gonzáles-Hernandes, L. Šmejkal, K. Výborný, Y. Yahagi, J. Sinova, T. Jungwirth, and J. Železný, Efficient electrical spin splitter based on nonrelativistic collinear antiferromagnetism, Phys. Rev. Lett. **126**, 127701 (2021).

[11] A. Bose, N. J. Schreiber, R. Jain, D. Shao, H. P. Nair, J. Sun, X. S. Zhang, D. A. Muller, E. Y. Tsymbal, D. G. Schlom, and D. C. Ralph, Tilted spin current generated by the collinear antiferromagnet ruthenium dioxide, Nat. Electron. **5**, 267 (2022).

[12] H. Bai, L. Han, X. Y. Feng, Y. J. Zhou, R. X. Su, Q. Wang, L. Y. Liao, W. X. Zhu, X. Z. Chen, F. Pan, X. L. Fan, and C. Song, Observation of spin splitting torque in a collinear antiferromagnet RuO_2, Phys. Rev. Lett. **128**, 197202 (2022).

[13] S. Karube, T. Tanaka, D. Sugawara, N. Kadoguchi, M. Kohda, and J. Nitta, Observation of spin-splitter torque in collinear antiferromagnetic RuO_2, Phys. Rev. Lett. **129**, 137201 (2022).

[14] H. Bai, Y. C. Zhang, Y. J. Zhou, P. Chen, C. H. Wan, L. Han, W. X. Zhu, S. X. Liang, Y. C. Su, X. F. Han, F. Pan, and C. Song, Efficient spin-to-charge conversion via altermagnetic spin splitting effect in antiferromagnet RuO_2, Phys. Rev. Lett. **130**, 216701 (2023).

[15] Y. Liu, H. Bai, Y. Song, Z. Ji, S. Lou, Z. Zhang, C. Song, and Q. Jin, Inverse altermagnetic spin splitting effect-induced terahertz emission in RuO_2, Adv. Opt. Mater. **11**, 2300177 (2023).

[16] M. Hiraishi, H. Okabe, A. Koda, R. Kadono, T. Muroi, D. Hirai, and Z. Hiroi, Nonmagnetic ground state in RuO_2 revealed by muon spin rotation, Phys. Rev. Lett. **132**, 166702 (2024).

[17] P. Keßler, L. Garcia-Gassull, A. Suter, T. Prokscha, Z. Salman, D. Khalyavin, P. Manuel, F. Orlandi, I. I. Mazin, R. Valentí, and S. Moser, Absence of magnetic order in RuO_2: Insights from μSR spectroscopy and neutron diffraction, Npj Spintron. **2**, 50 (2024).

[18] J. Liu, J. Zhan, T. Li, J. Liu, S. Cheng, Y. Shi, L. Deng, M. Zhang, Ch. Li, J. Ding, *et al.*, Absence of altermagnetic spin splitting character in rutile oxide RuO_2, Phys. Rev. Lett. **133**, 176401 (2024).

[19] S. Noh, G.-H. Kim, J. Lee, H. Jung, U. Seo, G. So, J. Lee, S. Lee, M. Park, S. Yang, *et al.*, Tunneling magnetoresistance in altermagnetic RuO_2-based magnetic tunnel junctions, Phys. Rev. Lett. **134**, 246703 (2025).

[20] J. Song, S. H. Lee, S. Kang, D. Kim, J. H. Jeong, T. Oh, S. Lee, S. Lee, S. Lee, K.-H. Ahn, *et al.*, Spin-orbit coupling driven magnetic response in altermagnetic RuO_2, Small **21**, 2407722 (2025).

[21] S. G. Jeong, S. Lee, B. Lin, Z. Yang, I. H. Choi, J. Y. Oh, S. Song, S. W. Lee, S. Nair, R. Choudhary, *et al.*, Metallicity and anomalous Hall effect in epitaxially-strained, atomically-thin RuO_2 films, arXiv:2501.11204.

[22] O. Fedchenko, J. Minár, A. Akashdeep, S. W. D'Souza, D. Vasilyev, O. Tkach, L. Odenbreit, Q. Nguyen, D. Kutnyakhov, N. Wind, *et al.*, Observation of time-reversal symmetry breaking in the band structure of altermagnetic RuO_2, Sci. Adv. **10**, eadj4883 (2024).

[23] Y. Fan, Q. Wang, W. Wang, D. Wang, Q. Huang, Z. Wang, X. Han, Y. Chen, L. Bai, S. Yan, and Y. Tian, Robust magnetic-field-free perpendicular magnetization switching by manipulating spin polarization direction in RuO_2/[Pt/Co/Pt] heterojunctions, ACS Nano. **18**, 26350 (2024).

[24] M. Weber, S. Wust, L. Haag, A. Akashdeep, K. Leckron, Ch. Schmitt, R. Ramos, T. Kikkawa, E. Saitoh, M. Kläui, *et al.*, All optical excitation of spin polarization in d-wave altermagnets, arXiv:2408.05187.

[25] Y.-C. Wang, Z.-Y. Shen, C.-H. Lin, W.-C. Hsu, Y.-Y. Chin, A. Kr. Singh, W.-L. Lee, S.-Y. Huang, and D. Qu, Absence of transport altermagnetic spin-splitting effect in RuO_2, Nano Lett. (2026).

[26] Z. Q. Wang, Z. Q. Li, L. Sun, Z. Y. Zhang, K. He, H. Niu, J. Cheng, M. Yang, X. Yang, G. Chen, *et al.*, Inverse spin Hall effect dominated spin-charge conversion in (101) and (110)-oriented RuO_2 films, Phys. Rev. Lett. **133**, 046701 (2024).

[27] D. T. Plouff, L. Scheuer, S. Shrestha, W. Wu, N. J. Parvez, S. Bhatt, X. Wang, L. Gundlach, M. B. Jungfleisch, and J. Q. Xiao, Revisiting altermagnetism in RuO_2: A study of laser-pulse induced charge dynamics by time-domain terahertz spectroscopy, Npj Spintron. **3**, 17 (2025).

[28] P. Kubaščík, R. Schlitz, O. Gueckstock, O. Franke, M. Borchert, G. Jakob, K. Olejník, A. Farkaš, Z. Kašpar, J. Jechumtál, *et al.*, Observation of terahertz spin-Hall magnetoresistance in insulating magnet YIG/Pt, arXiv:2507.02498.

[29] L. Nádvorník, M. Borchert, L. Brandt, R. Schlitz, K. A. de Mare, K. Výborný, I. Mertig, G. Jakob, M. Kläui, S. T. B. Goennenwein, *et al.*, Broadband terahertz probes of anisotropic magnetoresistance disentangle extrinsic and intrinsic contributions, Phys. Rev. X **11**, 021030 (2021).

[30] J. Jechumtál, R. Rouzegar, O. Gueckstock, Ch. Denker, W. Hoppe, Q. Remy, T. S. Seifert, P. Kubaščík, G. Woltersdorf, P. W. Brouwer, *et al.*, Accessing ultrafast spin-transport dynamics in Copper using broadband terahertz spectroscopy, Phys. Rev. Lett. **132**, 226703 (2024).

[31] T. S. Seifert, L. Cheng, Z. Wei, T. Kampfrath, and J. Qi, Spintronic sources of ultrashort terahertz electromagnetic pulses, Appl. Phys. Lett. **120**, 180401 (2022).

[32] R. Rouzegar, L. Brandt, L. Nádvorník, D. A. Reiss, A. L. Chekhov, O. Gueckstock, C. In, M. Wolf, T. S. Seifert, P. W. Brouwer, G. Woltersdorf, and T. Kampfrath, Laser-induced terahertz spin transport in magnetic nanostructures arises from the same force as ultrafast demagnetization, Phys. Rev. B **106**, 144427 (2022).

[33] O. Gueckstock, R. L. Seeger, T. S. Seifert, S. Auffret, S. Gambarelli, J. N. Kirchhof, K. I. Bolotin, V. Baltz, T. Kampfrath, and L. Nádvorník, Impact of gigahertz and terahertz transport regimes on spin propagation and conversion in the antiferromagnet IrMn, Appl. Phys. Lett. **120**, 062408 (2022).

[34] See Supplemental Material at http://link.aps.org/supplemental/10.1103/d17q-1lg4 for the figure of full $S_x(t)$ and $S_y(t)$ of all three samples and their spectra for samples containing RuO_2, TiO_2 refractive index measurement, time degradation of sample's signal modulation, SQUID characterization of magnetization of CoFeB layers, table with conductivities of used samples in two main axes, sample growth characterization note, detail on the spin Hall angle evaluation including model of optical power absorption and description of the RuO_2 (100) emission model, which also contains Refs. [33,53–60].

[35] T. Kampfrath, J. Nötzold, and M. Wolf, Sampling of broadband terahertz pulses with thick electro-optic crystals, Appl. Phys. Lett. **90**, 231113 (2007).

[36] D. Yagodkin, L. Nádvorník, O. Gueckstock, C. Gahl, T. Kampfrath, and K. I. Bolotin, Ultrafast photocurrents in $MoSe_2$ probed by terahertz spectroscopy, 2D Mater. **8**, 025012 (2021).

[37] L. Nádvorník, O. Gueckstock, L. Braun, Ch. Niu, J. Gräfe, G. Richter, G. Schütz, H. Takagi, M. Zeer, T. S. Seifert, *et al.*, Terahertz spin-to-charge current conversion in stacks of ferromagnets and the transition-metal dichalcogenide $NbSe_2$, Adv Mater. Inter. **9**, 2201675 (2022).

[38] M. Obstbaum, M. Härtinger, H. G. Bauer, T. Meier, F. Swientek, C. H. Back, and G. Woltersdorf, Inverse spin Hall effect in $Ni_{81}Fe_{19}$/normal-metal bilayers, Phys. Rev. B **89**, 060407(R) (2014).

[39] H. L. Wang, C. H. Du, Y. Pu, R. Adur, P. C. Hammel, and F. Y. Yang, Scaling of spin Hall angle in 3D, 4D, and 5D metals from $Y_3Fe_5O_{12}$/metal spin pumping, Phys. Rev. Lett. **112**, 197201 (2014).

[40] M. Isasa, E. Villamor, L. E. Hueso, M. Gradhand, and F. Casanova, Temperature dependence of spin diffusion length and spin Hall angle in Au and Pt, Phys. Rev. B **91**, 024402 (2015).

[41] J. Sinova, S. O. Valenzuela, J. Wunderlich, C. H. Back, and T. Jungwirth, Spin Hall effects, Rev. Mod. Phys. **87**, 1213 (2015).

[42] K. Kanehara, T. Hoshina, H. Takeda, and T. Tsurumi, Terahertz permittivity of rutile TiO_2 single crystal measured by anisotropic far-infrared ellipsometry, J. Ceram. Soc. Japan **123**, 303 (2015).

[43] N. Matsumoto, T. Hosokura, K. Kageyama, H. Takagi, Y. Sakabe, and M. Hangyo, Analysis of dielectric response of TiO_2 in terahertz frequency region by general harmonic oscillator model, Jpn. J. Appl. Phys. **47**, 7725 (2008).

[44] P. Kubaščík, A. Farkaš, K. Olejník, T. Troha, M. Hývl, F. Krizek, D. C. Joshi, T. Ostatnický, J. Jechumtál, M. Surýnek, *et al.*, Terahertz probing of anisotropic conductivity and morphology of CuMnAs epitaxial thin films, Adv. Phys. Res. **3**, 2300075 (2023).

[45] F. Zheng, M. Zhu, J. Dong, X. Li, Y. Zhou, K. Wu, and J. Zhang, Anatomy of the spin Hall effect in ferromagnetic metals, Phys. Rev. B **109**, 224401 (2024).

[46] F. Zheng, J. Dong, Y. Song, M. Zhu, X. Li, and J. Zhang, Spin Hall effect in 3d ferromagnetic metals for field-free switching of perpendicular magnetization: A first-principles investigation, Appl. Phys. Lett. **126**, 092408 (2025).

[47] Q. Zhang, Z. Luo, H. Li, Y. Yang, X. Zhang, and Y. Wu, Terahertz emission from anomalous Hall effect in a single-layer ferromagnet, Phys. Rev. Appl. **12**, 054027 (2019).

[48] F. Zheng, W. Tan, Z. Jin, Y-J. Chen, Z. Zhong, L. Zhang, S. Sun, J. Tang, Y. Jiang, P.-H. Wu, *et al.*, Anomalous nernst effect induced terahertz emission in a single ferromagnetic film, Nano Lett. **23**, 8171 (2023).

[49] O. Gueckstock, L. Nádvorník, M. Gradhand, T. S. Seifert, G. Bierhance, R. Rouzegar, M. Wolf, M. Vafaee, J. Cramer, M. A. Syskaki, *et al.*, Terahertz spin-to-charge conversion by interfacial skew scattering in metallic bilayers, Adv. Mater. **33**, 2006281 (2021).

[50] A. Smolyanyuk, I. I. Mazin, L. Garcia-Gassull, and R. Valentí, Fragility of the magnetic order in the prototypical altermagnet RuO_2, Phys. Rev. B **109**, 134424 (2024).

[51] E. Uykur, O. Janson, V. A. Ginga, M. Schmidt, N. Giordano, and A. A. Tsirlin, Tunable Dirac nodal line in orthorhombic RuO_2, Phys. Rew. B **111**, 134144 (2025).

[52] J. Jechumtál, O. Gueckstock, K. Jasenský, Z. Kašpar, K. Olejník, M. Gaerner, G. Reiss, S. Moser, P. Kessler, G. De Luca, S. Ganguly, J. Santiso, D. Scheffler, J. Zázvorka, P. Kubaščík, H. Reichlova, E. Schmoranzerova, P. Němec, T. Jungwirth, P. Kužel, T. Kampfrath, and L. Nádvorník, Data for Spin-to-charge-current conversion in altermagnetic candidate RuO_2 probed by terahertz emission spectroscopy [Data set], Zenodo (2025), https://doi.org/10.5281/zenodo.16882619.

[53] M. Born and E. Wolf, *Principles of Optics*, 7th ed. (Cambridge University Press, Cambridge, 1999), Sec. 1.6, p. 54.

[54] R. Jacobsson, *Progress in Optics*, edited by E. Wolf (North-Holland Publishing Co., Amsterdam, 1965), Chap. 5, p. 255.

[55] J. D. Jackson, *Classical Electrodynamics*, 3rd ed. (Wiley, New York, 1999), Sec. 6.8, p. 262.

[56] J. R. DeVore, Refractive indices of rutile and sphalerite, J. Opt. Soc. Am. **41**, 416 (1951).

[57] X. Lieang, X. Xu, R. Zheng, Z. A. Lum, and J. Qiu, Optical constant of CoFeB thin film measured with the interference enhancement method, Appl. Opt. **54**, 1557 (2015).

[58] A. K. Goel, G. Skorinko, and F. H. Pollak, Optical properties of single-crystal rutile RuO_2 and IrO_2 in the range 0.5 to 9.5 eV, Phys. Rev. B **24**, 7342 (1981).

[59] W. S. M. Werner, K. Glantschnig, and C. Ambrosch-Draxl, Optical constants and inelastic electron-scattering data for 17 elemental metals, J. Phys. Chem. Ref. Data **38**, 1013 (2009).

[60] C. Schinke, P. Ch. Peest, J. Schmidt, R. Brendel, K. Bothe, M. R. Vogt, I. Kröger, S. Winter, A. Schirmacher, S. Lim, H. T. Nguyen, and D. MacDonald, Uncertainty analysis for the coefficient of band-to-band absorption of crystalline silicon, AIP Adv. **5**, 67168 (2015).